A Parameter Recognition-Based Impedance Tuning Method for SS-Compensated Wireless Power Transfer Systems

Gangwei Zhu, *Student Member, IEEE*, Jianning Dong, *Senior Member, IEEE*, Francesca Grazian, *Student Member, IEEE*, and Pavol Bauer, *Senior Member, IEEE*

***Abstract*—This article presents a parameter recognition-based impedance tuning method for the impedance mismatch caused by capacitance drift and coil misalignment in series–series-compensated wireless power transfer (WPT) systems. First, a parameter recognition method is proposed to identify the unknown parameters of the resonant circuits by only measuring the rms values of the coil currents. No phase detection circuits and auxiliary measurement coils are required. Furthermore, according to the recognized parameters, the reactance on both sides are minimized simultaneously by regulating the system frequency and the phase shift angles of the active rectifier. Compared with the existing methods, the proposed parameter recognition method adopts a dynamic frequency approaching strategy to avoid severe system detuning due to the bifurcation phenomenon. Moreover, based on the recognized parameters, the proposed impedance tuning method can simultaneously cope with the parameter deviations caused by capacitance drift and coil misalignment on both sides without using extra circuits and switches. Experimental results show that the unknown parameters of the resonant circuits are recognized accurately, with the average relative errors all less than 3%. Additionally, by implementing the impedance tuning method, the dc to dc efficiency of the WPT prototype is improved by 4.3%–15% in the experiments.**

***Index Terms*—Capacitance drift, coil misalignment, impedance tuning, parameter recognition, wireless power transfer (WPT).**

I. Introduction

As an emerging technology in recent decades, wireless power transfer (WPT) enables safe, convenient, and automated charging in many industrial applications, such as portable electronics [1], underwater loads [2], implanted medical devices [3], and electric vehicles [4], [5], [6]. To obtain a higher transmission efficiency, various compensation topologies are introduced in WPT systems to cancel the leakage inductance of the loosely coupled coils, where the most widely used one is the series–series (SS) compensation [7]. In the SS-compensated WPT system, the series capacitors are designed to be resonant with the coils at the nominal resonant frequency. However, due to the component tolerances, temperature variations and aging effects, the compensation capacitance may deviate from the nominal values [8]. Additionally, in practical WPT applications, the metallic shielding plates are usually used in the transmitter (Tx) and receiver (Rx) coils to protect human and electronic devices from the stray magnetic field, while magnetic ferrites are often employed to improve the coil coupling. As a result, the self-inductances of the coils become sensitive to the spatial displacement between the Tx and Rx pads as these metallic and magnetic materials interfere with the transmission of the magnetic flux [9]. The parameter deviations caused by the capacitance drift and coil misalignment lead to detuning of the system, which reduces the transmission efficiency and results in a lower power factor [10]. Therefore, in order to obtain better transmission performance, it is desirable for the system to consistently operate at the resonance state regardless of the capacitance drift and coil misalignment.

Many works have been done to deal with the impedance mismatch caused by parameter deviations, which can be roughly divided into three categories:

1) using the variable capacitors or inductors [9], [11], [12], [13], [14], [15];
2) tracking the resonant frequency [16], [17];
3) adopting the active rectifier [18], [19].

A commonly used approach for impedance tuning is to adjust the compensation impedance. In [11], a variable inductor was implemented in the secondary side to dynamically tune the receiver circuit. However, two extra conversion stages, i.e., a diode rectifier and a buck converter, are required in this method, which greatly increases the hardware costs. In [12], [13], and [14], by introducing the selectable capacitor array, the compensation capacitance is discretely regulated. Nevertheless, the use of numerous switches and capacitors increases the system volume and costs. Additionally, this method fails to continuously adjust the impedance. To reduce the number of components and realize continuous tuning, controllable capacitors were used in [9] and [15]. In [15], a voltage-controlled capacitor was proposed to achieve dynamic impedance tuning. Nevertheless,

Manuscript received 6 December 2022; revised 22 March 2023, 17 May 2023, and 28 June 2023; accepted 1 August 2023. Date of publication 4 August 2023; date of current version 22 September 2023. This work was supported by China Scholarship Council (CSC) under Grant 202106230112. The work of Gangwei Zhu at the Delft University of Technology in the Netherlands was supported by the CSC. Recommended for publication by Associate Editor Ming Liu. *(Corresponding author: Gangwei Zhu.)*

The authors are with the DC System, Energy Conversion and Storage (DCE&S) Group, Faculty of Electrical Engineering, Mathematics and Computer Science (EEMCS), Delft University of Technology, 2624 CP Delft, Netherlands (e-mail: g.zhu-2@tudelft.nl; j.dong-4@tudelft.nl; f.grazian@tudelft.nl; p.bauer@tudelft.nl).

Color versions of one or more figures in this article are available at https://doi.org/10.1109/TPEL.2023.3302256.

Digital Object Identifier 10.1109/TPEL.2023.3302256

the analog amplifier used in this method limits the power transfer capability, and thus, it is only suitable for applications of a few watts. In [9], a pulsewidth modulation (PWM) controlled capacitor was proposed to withstand the detuning caused by the Tx inductance variation. This method enables continuous capacitance tuning and is able to cope with high-power applications. However, the introduction of additional power switches in the PWM-controlled capacitors increases the power losses and hardware costs. Additionally, the capacitance drift is not considered in this method.

Another typical method to deal with the impedance mismatch is to track the resonant frequency. In [16], a power-frequency controller was proposed, which implements the resonance tracking by synchronizing the switching signals with the resonant current. In [17], a self-oscillating switching technique was adopted, where the switching frequency of the inverter automatically tracks the resonant frequency. However, these methods can only realize zero-phase-angle (ZPA) input, whereas the reactance in the Rx side cannot be tuned.

To tune the Rx-side reactance, the active control of the rectifier was adopted in some methods. In [18] and [19], by regulating the duty cycle and the phase shift angle of the active rectifier, the equivalent load impedance was regulated to minimize the Rx-side reactance and to realize the maximum efficiency tracking. However, the active rectifier control cannot simultaneously handle the impedance mismatch on both sides.

Recently, some researchers combine the resonant frequency tracking and the active rectifier control to tune the reactance on both the Tx and Rx sides. In [20], an impedance tuning control was proposed to deal with the self-inductance variations caused by coil misalignment, where the switching frequency was controlled to realize ZPA input and a synchronous switching technique was proposed for the active rectifier to minimize the Rx-side reactance. However, the parameter deviations caused by capacitance drift were not discussed in this method. In [21], an impedance decoupling-based method was proposed to minimize the dual-side reactance caused by capacitance drift. Nevertheless, the phase detection circuits and an auxiliary measurement coil are needed to measure the reactance angles on both sides, which increases the hardware costs and complexity.

The phase detection circuits for reactance angle measurements can be avoided by parameter recognition. Dai et al. [22] presented a pulse density modulation-based parameter identification method to simultaneously estimate the self-inductance and compensation capacitance on the Rx-side. However, only the Rx-side reactance is tuned in this method. In [23], a parameter recognition-based self-tuning method was proposed to address a wide range of coupling coefficient variations, where both the mutual inductance and the self-inductances can be identified without using the phase information and auxiliary measurement coils. However, this method cannot identify the compensation capacitances.

In practice, the impedance mismatch usually involves deviations of multiple parameters, and it is challenging to tune the impedance when considering all of them. Therefore, previous studies mainly focus on parameter deviations in one specific aspect, for instance, only considering the coil misalignment [9], [20], [23], [24], [25], the capacitance drift [21], or the impedance mismatch on just one side [22]. To simultaneously tune the dual-side impedance mismatch under capacitance drift and coil misalignment, the parameters of the whole resonant circuit are required to be identified. Although the identification of multiple parameters can be realized by the frequency-sweep-based front-end monitoring methods [26], [27], these methods generally sweep the frequency around the nominal resonant frequency, which leads to severe system detuning and significant load power ripple especially under parameter deviations.

To fill up the aforementioned research gaps, this article proposes a new parameter recognition-based impedance tuning method. First, a parameter recognition method is proposed to identify the unknown parameters of the resonant circuits, and the original features of this method are summarized as follows.

1) Compared to the conventional front-end parameter monitoring methods, the secondary-side information is introduced, and therefore, all of the unknown parameters of the resonant circuits, including the self-inductances, the mutual inductance, and the compensation capacitances, are recognized accurately, without using any phase detection circuits and auxiliary measurement coils.
2) A dynamic frequency approaching strategy is proposed to acquire the required data for parameter recognition, which avoids severe system detuning during the traditional frequency-sweep process.
3) The parameter recognition is implemented at pre start-up, with the rectifier output short-circuited during this process, which avoids significant load power fluctuations caused by frequency variations.
4) A simple yet powerful heuristic algorithm called JAYA is introduced to recognize the unknown parameters. Compared with the conventional genetic algorithm (GA) and differential evolution (DE) algorithm, which need to tune the parameters of the differential weight and the crossover rate, the JAYA algorithm is free from algorithm-specific parameters and thereby avoids the difficulty of tuning parameters [28].

Furthermore, based on the recognized parameters, the reactance on both sides are minimized simultaneously by regulating the system frequency and the phase-shift angles of the active rectifier.

The rest of this article is organized as follows. Section II introduces the configuration of the SS-compensated system and analyses the impact of the impedance mismatch caused by capacitance drift and coil misalignment. In Section III, the proposed parameter recognition method is described, and the corresponding impedance tuning method is presented. In Section IV, experimental results are given to validate this proposal. Finally, Section V concludes this article.

II. Impedance Mismatch Caused by Capacitance Drift and Coil Misalignment

A. System Configuration

As shown in Fig. 1, a typical SS-compensated WPT system is studied in this article, where an active rectifier is adopted in the

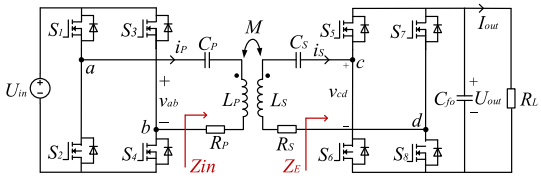

Fig. 1. Circuit diagram of the SS-compensated WPT system using the active rectifier.

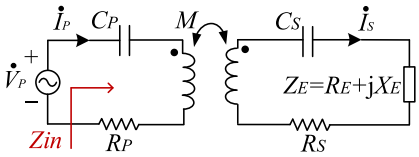

Fig. 2. Equivalent circuit model of the WPT system.

secondary side. The dc input voltage is represented by U_{in}, while the dc output voltage and current are denoted by U_{out} and I_{out}, respectively. Moreover, v_{ab} and v_{cd} are the ac voltages of the inverter and rectifier; i_P and i_S are the transmitter and receiver coil currents; L_P and L_S represent the self-inductances of the coupled coils; C_P and C_S are their corresponding compensation capacitors; R_P and R_S are the equivalent loss resistances of the primary and secondary resonant circuits; and R_L is the resistive load. The mutual inductance of the coils is denoted by $M = k\sqrt{L_P L_S}$, where k is the coupling coefficient. The equivalent circuit model derived by fundamental frequency approximation is further presented in Fig. 2, where Z_E is the equivalent load impedance regulated by the active rectifier; $\dot{V}_P$, $\dot{I}_P$, and $\dot{I}_S$ are the phasor forms of the fundamental components of v_{ab}, i_P, and i_S, respectively. According to the Kirchhoff's voltage law, the steady-state equation of the system is given by

$$\begin{cases} \dot{V}_P = Z_P \dot{I}_P - j\omega M \dot{I}_S \\ 0 = j\omega M \dot{I}_P - (Z_S + Z_E)\dot{I}_S. \end{cases} \tag{1}$$

The equivalent impedances of primary and secondary resonant circuits Z_P and Z_S are expressed as

$$Z_i = R_i + jX_i, X_i = \omega L_i - 1/(\omega C_i) \tag{2}$$

where the subscript i indicates the primary (P) or the secondary (S) side. Moreover, the equivalent load impedance Z_E is represented by $Z_E = R_E + jX_E$, where R_E and X_E are the equivalent load resistance and reactance, respectively.

B. Parameter Deviations Caused by Coil Misalignment and Capacitance Drift

Ideally, for the SS-compensated WPT system, the compensation capacitors are designed to resonate with the coupled coils at the nominal resonant frequency. Nevertheless, in practical applications, the parameters of the resonant circuits may deviate from the nominal values due to the coil misalignment and capacitance drift.

On one hand, as the aluminum shielding sheets and magnetic ferrites are generally used in the Tx and Rx pads, the coil self-inductances vary with the spatial displacement. To demonstrate the impact of coil misalignment, the measured coil

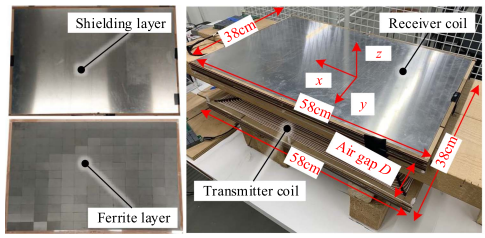

Fig. 3. Charging pads with the shielding and ferrite layers.

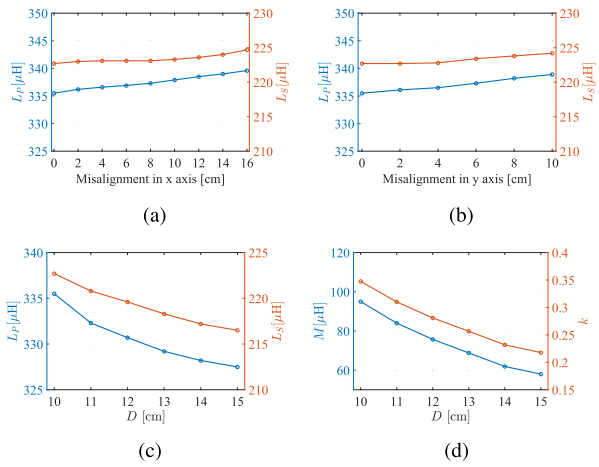

Fig. 4. Measured coil inductances under different coil misalignment directions and air gaps. (a) Self-inductance variations under the x-direction misalignment ($D = 10$ cm). (b) Self-inductance variations under the y-direction misalignment ($D = 10$ cm). (c) Self-inductance variations under different air gaps. (d) Variations in mutual inductance and coupling coefficient under different air gaps.

inductances under different misalignment directions and air gaps are illustrated in Fig. 4 for the charging pads shown in Fig. 3. As it can be observed from Fig. 4, the coil self-inductances slightly increase as the misalignment in the x- and y-directions increases. More significant inductance variations can be observed under different air gaps. As the air gap D increases from 10 to 15 cm, the primary self-inductance L_P drops from 335.5 to 327.5 μH, while the secondary self-inductance L_S decreases from 222.7 to 216.5 μH. Meanwhile, the increase in the air gap reduces the coupling coefficient k from 0.35 to 0.22. In this article, two cases, with the air gap D at 10 cm and 15 cm, are selected as cases A and B for theoretical analysis, respectively.

On the other hand, due to the ambient temperature variations, the aging effect, and the manufacturing errors, significant capacitance drift may occur in the practical applications. Therefore, it is essential to investigate the influence of the capacitance drift. In this article, both the primary and secondary capacitance deviations are considered and expressed as

$$C_P = (1 + d_P)C_{P0}, C_S = (1 + d_S)C_{S0} \tag{3}$$

where d_P and d_S indicate the degree of capacitance drift; and C_{P0} and C_{S0} are the nominal compensation capacitances. Considering component tolerances of the commercialized capacitors, the aging effects and the ambient temperature variations, the maximum degree of capacitance drift is set to $\pm 20\%$ to ensure

TABLE I
SYSTEM PARAMETERS OF THE SS-COMPENSATED WPT SYSTEM

Symbol	Parameters	Value	Unit
L_P	Primary coil inductance	327.5 $\sim$ 335.5	μH
L_S	Secondary coil inductance	216.5 $\sim$ 222.7	μH
k	Coupling coefficient	0.22 $\sim$ 0.35	/
C_{P0}	Nominal primary capacitance	10.45	nF
C_{S0}	Nominal secondary capacitance	15.74	nF
d_P	Degree of primary capacitance drift	-0.2$\sim$0.2	/
d_S	Degree of secondary capacitance drift	-0.2$\sim$0.2	/
R_P	Primary loss resistance	0.72	Ω
R_S	Secondary loss resistance	0.48	Ω
R_L	Load resistance	100	Ω
f_N	Nominal switching frequency	85	kHz
U_{in}	DC input voltage	200	V

that the proposed WPT system is able to deal with the majority of the capacitance drift cases in practice. The investigated capacitance drift range follows the analysis in [21].

With the parameter deviations caused by capacitance drift and coil misalignment taken into account, the parameters of the SS-compensated system are listed in Table I.

C. Impact of Parameter Deviations

1) Power Transfer Capability: According to (1), the output power of the resonant tank is derived by

$$P_{\text{out}} = |\dot{I}_S|^2 R_E = \omega^2 M^2 |\dot{V}_P|^2 R_E / D_E \tag{4}$$

where $D_E = (X_P^2 + R_P^2)(R_{ST}^2 + X_{ST}^2) + 2\omega^2 M^2 (R_P R_{ST} - X_P X_{ST}) + \omega^4 M^4$, $R_{ST} = R_S + R_E$, and $X_{ST} = X_S + X_E$. As illustrated in (4), the parameter deviations of the coil inductances and compensation capacitances influence the primary and secondary reactance X_P and X_S, which in turn affects the output power. Assume the equivalent load reactance $X_E = 0$, the output power P_{out} versus the equivalent load resistance R_E under parameter deviations is shown in Fig. 5. As it can be observed in Fig. 5(a), the output power curve has a peak point when the degree of capacitance drift is $d_P = d_S = -0.2$. This means that the power transfer capability of the system is limited no matter how the load resistance R_E is adjusted, and therefore, the system may not be able to reach the required output power. Similar power limitations can also be observed in Fig. 5(b). Compared with Case A, since the air gap D of Case B is increased from 10 to 15 cm, the mutual inductance is correspondingly reduced from 95 to 58 μH, and thus, the system can reach more power. However, in some cases, the output power of the system is still limited due to the capacitance drift, for example, the case of $d_P = 0.2, d_S = 0$.

2) Transfer Efficiency: Another effect of the parameter deviations is on the transfer efficiency. Based on (1), the transmission efficiency of the resonant tank is obtained as

$$\eta = \frac{|\dot{I}_S|^2 R_E}{\text{Re}[\dot{V}_P(\dot{I}_P)^*]} = \frac{\omega^2 M^2 R_E}{\omega^2 M^2 R_{ST} + R_P(R_{ST}^2 + X_{ST}^2)}. \tag{5}$$

As it can be observed in (5), the secondary lumped reactance X_{ST} that exists in the denominator degrades the transfer efficiency, whereas the primary reactance X_P does not directly affect the efficiency. Assume $X_E = 0$ and $d_P = 0$, the efficiency η versus the output power P_{out} under parameter deviations is shown in Fig. 6. As it can be observed in Fig. 6(a), the transfer efficiency of the resonant tank is degraded due to the capacitance drift, and the efficiency drop is more noticeable under light load conditions. Moreover, as shown in Fig. 6(b), since the air gap D is increased to 15 cm in Case B, the secondary self-inductance L_S is reduced from 222.7 to 216.5 μH. In this case, the secondary reactance X_S becomes larger when the secondary capacitance is also decreased, and thus, remarkable efficiency reduction can be observed when $d_S = -0.2$.

According to the aforementioned analysis, the parameter deviations caused by coil misalignment and capacitance drift reduce the system transfer efficiency and may result in a failure to obtain the required output power. Therefore, it is desirable to cancel the dual-side reactance caused by parameter deviations so that the system can always operate at the resonance state.

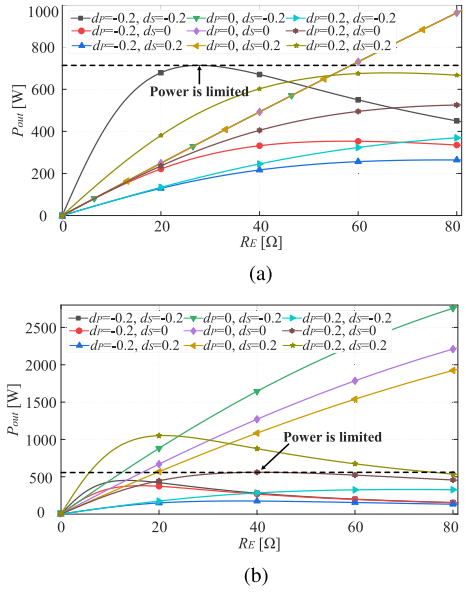

Fig. 5. Output power P_{out} versus the equivalent load resistance R_E under parameter deviations. (a) Case A. (b) Case B.

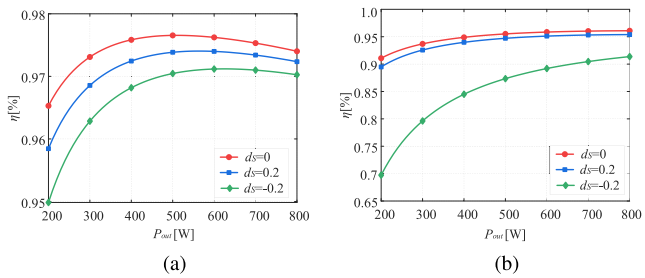

Fig. 6. Transfer efficiency η versus the output power P_{out} under parameter deviations. (a) Case A. (b) Case B. Herein, the equivalent load resistance R_E is adjusted to obtain the same output power under different values of d_S.

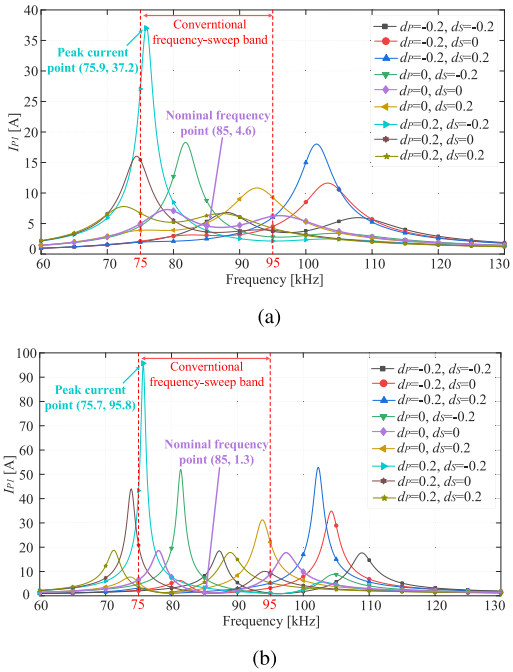

Fig. 7. Value of I_{P1} under frequency variations and parameter deviations. (a) $R_E = 24.1\,\Omega$ (Case B), where the output power at the nominal frequency point is 800 W. (b) $R_E = 5.8\,\Omega$ (Case B), where the output power at the nominal frequency point is 200 W. Herein, the DC input voltage of the system is 200 V, the nominal switching frequency is 85 kHz, and the inverter output is set to the full duty cycle.

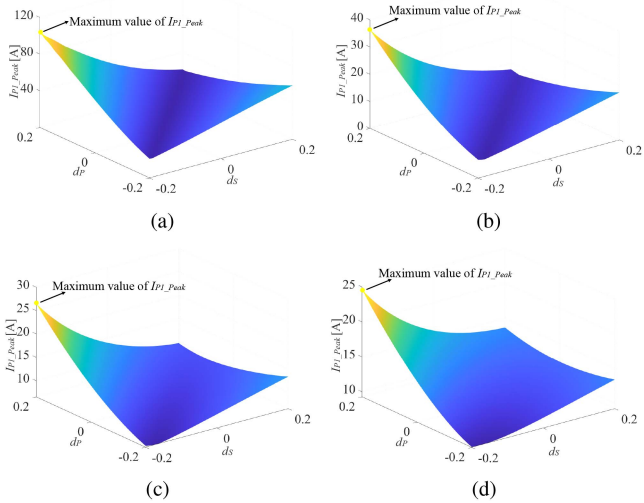

Fig. 8. Value of the peak primary coil current I_{P1_Peak} under different values of R_E and degree of capacitance drift in Case B. (a) $R_E = 5\,\Omega$. (b) $R_E = 25\,\Omega$. (c) $R_E = 45\,\Omega$. (d) $R_E = 65\,\Omega$.

III. Proposed Parameter Recognition-Based Impedance Tuning Method

A. System Detuning Caused by Frequency Variations

To identify the unknown parameters, conventional parameter recognition methods generally sweep the frequency around the nominal resonant frequency [26], [27]. However, for the SS-compensated WPT system, the nominal resonant frequency may split into multiple resonant frequencies due to the parameter deviations, which is the so-called bifurcation phenomenon [29]. Since these resonant frequencies are close to the nominal frequency, the traditional frequency-sweep process causes severe system detuning under parameter deviations, which results in enormous coil currents and significant power ripple.

To demonstrate the influence of the system detuning on the coil currents, the rms value of the fundamental component of the primary coil current I_{P1} under parameter deviations and frequency variations is depicted in Fig. 7, where the frequency-sweep band is set to 75∼95 kHz to ensure that sufficient frequency points can be collected [26]. In Fig. 7, the equivalent load resistance R_E is set to different values to investigate the impact of load variations, while Case B is selected as an example to demonstrate the influence of coil misalignment. Moreover, nine different capacitance drift cases are illustrated with dotted solid lines in different colors to show the influence of capacitance drift, where the maximum degree of capacitance drift is set to ±20%. As illustrated in Fig. 7(a), when the equivalent load resistance R_E is 24.1 Ω under Case B, the output power at the nominal frequency point is 800 W, with the primary coil current at 4.6 A. However, I_{P1} increases to 37.2 A at 75.9 kHz under $d_P = 0.2$ and $d_S = -0.2$. More severe system detuning can be observed under smaller load resistances, as shown in Fig. 7(b). When the equivalent load resistance R_E is 5.8 Ω under Case B, the output power at the nominal frequency point is 200 W, with the primary coil current I_{P1} at 1.3 A. Due to the frequency variations and capacitance drift, I_{P1} dramatically increases to 95.8 A at 75.7 kHz under $d_P = 0.2$ and $d_S = -0.2$. It should be noted that, in Fig. 7, the inverter output is set to the full duty cycle. Although decreasing the inverter duty cycle is able to reduce the coil currents, it results in a remarkable disparity in the current amplitudes under different cases. This poses a great challenge to the measurement accuracy of the coil currents.

Furthermore, observing the current curve in Fig. 7 reveals that the peak current point can be derived by sweeping the frequency. Take Case B as an example, by sweeping the frequency from 60 to 130 kHz, the peak value of the primary coil current I_{P1_Peak} under different values of R_E and degree of capacitance drift is illustrated in Fig. 8. As shown in Fig. 8, the maximum value of I_{P1_Peak}, i.e., MAX_$IP1$_Peak, can always be found in the case of $d_P = 0.2$ and $d_S = -0.2$, where the degree of the primary and secondary capacitance drift reaches the upper boundary and the lower boundary, respectively. Moreover, by sweeping the parameters of the equivalent load resistance R_E and the coil coupling coefficient k, the value of MAX_$IP1$_Peak under load variations and coupling changes is shown in Fig. 9. As it can be observed, the value of MAX_$IP1$_Peak is inversely related to both R_E and k. In other words, when R_E or k is small, more severe system detuning may occur due to the frequency variations and parameter deviations. Specifically, the worst case shown in Fig. 9 is the point A, where the value of MAX_$IP1$_Peak reaches 101.8 A when $R_E = 5\,\Omega$ and $k = 0.22$, while the best case is the point B, where the value of MAX_$IP1$_Peak is 11.6 A under $R_E = 81\,\Omega$ and $k = 0.35$.

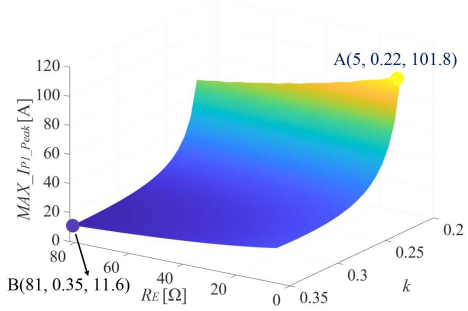

Fig. 9. Value of MAX_$IP1$_Peak under different values of R_E and k.

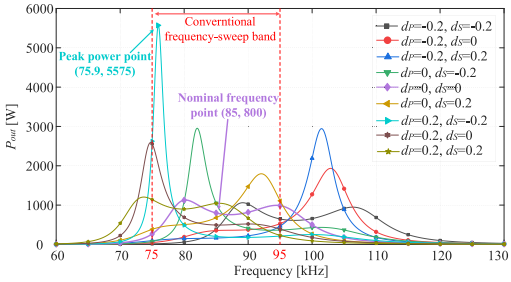

Fig. 10. System output power P_{out} under frequency variations and parameter deviations when the equivalent load resistance R_E is 24.1 Ω in Case B. Herein, the input conditions of the system are the same as those in Fig. 7.

The increased coil currents not only significantly increase the current stress of the resonant tank, but also potentially damage the semiconductor devices due to the rise of their junction temperature.

Another impact of the system detuning is on the system output power P_{out}. As shown in Fig. 10, when the equivalent load resistance R_E is 24.1 Ω under Case B, significant power ripple is observed under frequency variations and parameter deviations. In some cases, the output power of the system may considerably exceed the load tolerance, eventually causing irreparable damage to the load.

According to the aforementioned analysis, it can be concluded that the traditional frequency-sweep-based parameter recognition methods may lead to severe system detuning under parameter deviations, resulting in considerable coil currents and significant power ripple. Therefore, to ensure the safe operation of the system, it is essential to avoid wide frequency variations near the nominal resonance point.

B. Proposed Parameter Recognition Method

This article proposes a new parameter recognition method to recognize the unknown parameters of the capacitors and coils, i.e., L_P, L_S, C_P, C_S, and M, as shown in Fig. 11. First, the parameter recognition process is carried out at pre start-up, and the rectifier output is short-circuited during this process. As a result, significant load power ripple during the conventional frequency-sweep process is avoided. It should be noted that in [30] and [31], the rectifier output is also short-circuited to implement fast mutual inductance identification. However, in this article, all the unknown parameters of the resonant circuits

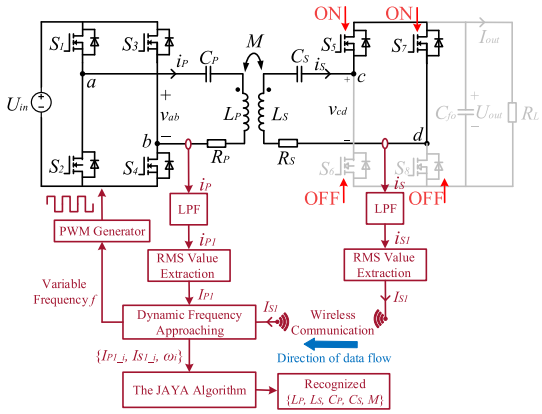

Fig. 11. Block diagram of the proposed parameter recognition method implemented at pre start-up, where the rectifier output is short-circuited during this process. Herein, the measured I_{S1} is transmitted from the secondary controller to the primary controller for parameter recognition.

are considered, and the number of unknown parameters are much larger than that in [30] and [31]. Then, the primary and secondary coil currents i_P and i_S are measured and fed to two separate low-pass filters (LPFs). With the LPFs, the fundamental components of i_P and i_S, i.e., i_{P1} and i_{S1}, are extracted. Furthermore, the rms values of i_{P1} and i_{S1}, i.e., I_{P1} and I_{S1}, are obtained by the rms value extraction modules. According to the values of I_{P1} and I_{S1}, a dynamic frequency approaching strategy is proposed to determine the selected frequency points. By recording the values of I_{P1} and I_{S1} at different frequency points, multiple sets of $\{\omega_i, I_{P1\_i}, I_{S1\_i}\}$ are acquired. Finally, based on the acquired data, the unknown parameters are derived by the JAYA algorithm. In the following section, the implementation of the proposed method will be described in detail.

1) Recognition Model: When the rectifier output is short-circuited, the equivalent input impedance Z_{in} of the SS-compensated system is derived by

$$Z_{\text{in}} = R_P + j\left(\omega L_P - \frac{1}{\omega C_P}\right) + Z_R \tag{6}$$

where Z_R is the reflected impedance of the secondary resonant circuit, which can be expressed as

$$Z_R = \frac{(\omega M)^2}{R_S + j[\omega L_S - 1/(\omega C_S)]}. \tag{7}$$

The amplitude of the equivalent input impedance is denoted by $|Z_{\text{in}}|$. If the switching angular frequency ω is switched to another value, a new value of $|Z_{\text{in}}|$ can be obtained. Furthermore, by sweeping the switching frequency ω, multiple sets of $\{\omega_i, |Z_{\text{in\_}i}|\}$ can be acquired as

$$|Z_{\text{in\_}i}| = \frac{V_{P1\_i}}{I_{P1\_i}} = f(R_P, R_S, L_P, L_S, C_P, C_S, M, \omega_i) \tag{8}$$

where $\omega_i (i = 1, 2, \ldots, m)$ is the ith selected frequency point; m is the number of the measured frequency points; V_{P1_i} and I_{P1_i} are the rms values of v_{P1} and i_{P1} at the ith frequency point; and v_{P1} is the fundamental component of the inverter output voltage v_{ab}. According to the analysis in [26], assuming R_P and R_S are

given, $\{L_P, L_S, C_P, C_S, M\}$ can be estimated by multiple sets of $\{\omega_i, |Z_{in\_i}|\}$.

However, it is difficult to identify $\{L_S, C_S, M\}$ accurately with only the front-end information, as there are countless sets of $\{L_S, C_S, M\}$ that lead to an almost consistent reflected impedance Z_R. Suppose there is a new set of solution $\{L'_S, C'_S, M'\}$ satisfying $L'_S = \lambda L_S$, $C'_S = (1/\lambda)C_S$, $M' = \sqrt{\lambda}M$, where $\{L_S, C_S, M\}$ represents the correct solution and λ is any nonzero positive real number. Generally, when the switching frequency ω is deviated from the secondary resonant frequency ω_S ($\omega_S = 1/\sqrt{L_S C_S}$), X_S is much larger than R_S. Therefore, the reflected impedance Z'_R of the new set of solution satisfies

$$Z'_R \approx \frac{(\omega M')^2}{j[\omega L'_S - 1/(\omega C'_S)]} = \frac{\lambda(\omega M)^2}{j\lambda[\omega L_S - 1/(\omega C_S)]} \approx Z_R. \tag{9}$$

Since λ can be any value, there are countless sets of solution $\{L'_S, C'_S, M'\}$ such that the reflected impedance Z'_R is almost identical with the correct reflected impedance Z_R. This means that it is difficult to accurately recognize $\{L_S, C_S, M\}$ with only the primary-side information. Therefore, in this article, the secondary coil current i_S is also measured. By introducing the secondary-side information, the relationship between I_{S1} and I_{P1} is established as

$$\frac{I_{P1}}{I_{S1}} = \sqrt{\frac{R_S^2 + [\omega L_S - 1/(\omega C_S)]^2}{(\omega M)^2}} \approx \frac{\omega L_S - 1/(\omega C_S)}{\omega M}. \tag{10}$$

Define the ratio of I_{P1} to I_{S1} as T_{ii}, i.e., $T_{ii} = I_{P1}/I_{S1}$. Then, the ratio T'_{ii} of the new set of solution $\{L'_S, C'_S, M'\}$ satisfies

$$T'_{ii} \approx \frac{\omega L'_S - 1/(\omega C'_S)}{\omega M'} = \frac{\lambda[\omega L_S - 1/(\omega C_S)]}{\sqrt{\lambda}\omega M} \approx \sqrt{\lambda} T_{ii}. \tag{11}$$

The only solution of λ such that (9) and (11) hold simultaneously is $\lambda = 1$. This means that by introducing the information of i_S, the correct solution of $\{L_S, C_S, M\}$ is unique and all the unknown parameters can be estimated accurately.

To introduce the information of i_S into the recognition model, the equivalent gain from I_{S1} to V_{P1} is given by

$$|Z_{PS}| = \frac{V_{P1}}{I_{S1}} = \left| j\omega M - \frac{(R_P + jX_P)(R_S + jX_S)}{j\omega M} \right|. \tag{12}$$

Similarly, by sweeping the switching frequency ω, multiple sets of $\{\omega_i, |Z_{PS\_i}|\}$ can be obtained as

$$|Z_{PS\_i}| = \frac{V_{P1\_i}}{I_{S1\_i}} = g(R_P, R_S, L_P, L_S, C_P, C_S, M, \omega_i). \tag{13}$$

Furthermore, with the information on both sides, the recognition model for the unknown parameters is derived as

$$\min J = ||\boldsymbol{V_{P1}} - \boldsymbol{V_{P1\text{est}}}|| + ||\boldsymbol{V_{P1}} - \hat{\boldsymbol{V}}_{\boldsymbol{P1\text{est}}}|| \tag{14}$$

s.t. $\boldsymbol{V_{P1\text{est}}} = |\boldsymbol{Z}_{\text{in}}|\boldsymbol{I_{P1}}$, $\hat{\boldsymbol{V}}_{\boldsymbol{P1\text{est}}} = |\boldsymbol{Z_{PS}}|\boldsymbol{I_{S1}}$, $L_{PL} \le L_P \le L_{PH}$, $L_{SL} \le L_S \le L_{SH}$, $C_{PL} \le C_P \le C_{PH}$, $C_{SL} \le C_S \le C_{SH}$, and $M_L \le M \le M_H$, where

$$|\boldsymbol{Z}_{\text{in}}| = \text{diag}\{|Z_{\text{in\_}i}|\}(i = 1, \ldots, m)$$

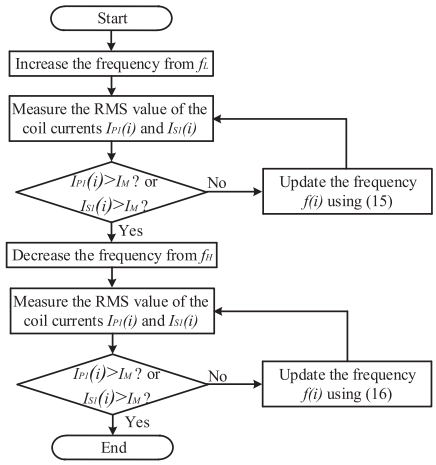

Fig. 12. Flow chart of the proposed dynamic frequency approaching strategy.

$$|\boldsymbol{Z_{PS}}| = \text{diag}\{|Z_{PS\_i}|\}(i = 1, \ldots, m)$$
$$\boldsymbol{I_{P1}} = [I_{P1\_1}, I_{P1\_2}, \ldots, I_{P1\_m}]$$
$$\boldsymbol{I_{S1}} = [I_{S1\_1}, I_{S1\_2}, \ldots, I_{S1\_m}]$$
$$\boldsymbol{V_{P1\text{est}}} = [V_{P1\text{est}\_1}, V_{P1\text{est}\_2}, \ldots, V_{P1\text{est}\_m}]$$
$$\hat{\boldsymbol{V}}_{\boldsymbol{P1\text{est}}} = \left[\hat{V}_{P1\text{est}\_1}, \hat{V}_{P1\text{est}\_2}, \ldots, \hat{V}_{P1\text{est}\_m}\right]$$
$$\boldsymbol{V_{P1}} = [V_{P1\_1}, V_{P1\_2}, \ldots, V_{P1\_m}].$$

Herein, $\boldsymbol{I_{P1}}$ is the measured rms values of i_{P1} at multiple frequency points; $\boldsymbol{V_{P1\text{est}}}$ is the estimated rms values of v_{P1} derived by $|\boldsymbol{Z}_{\text{in}}|\boldsymbol{I_{P1}}$; $\boldsymbol{I_{S1}}$ is the measured rms values of i_{S1}; $\hat{\boldsymbol{V}}_{\boldsymbol{P1\text{est}}}$ is the estimated rms values of v_{P1} derived by $|\boldsymbol{Z_{PS}}|\boldsymbol{I_{S1}}$; $\boldsymbol{V_{P1}}$ is the measured rms values of v_{P1}; $||\boldsymbol{V_{P1}} - \boldsymbol{V_{P1\text{est}}}||$ represents the norm of the voltage differences between $\boldsymbol{V_{P1}}$ and $\boldsymbol{V_{P1\text{est}}}$; $||\boldsymbol{V_{P1}} - \hat{\boldsymbol{V}}_{\boldsymbol{P1\text{est}}}||$ is the norm of the voltage differences between $\boldsymbol{V_{P1}}$ and $\hat{\boldsymbol{V}}_{\boldsymbol{P1\text{est}}}$. It should be noted that when the dc input voltage U_{in} and the duty cycle of the inverter ac voltage v_{ab} remain unchanged, the rms value of v_{P1} does not vary with the switching frequency. In our article, the dc input voltage is configured at 200 V, and the inverter output is fixed at the full duty cycle. This means that the measurement process for the inverter voltage can be avoided. Based on the recognition model, the unknown parameters $\{L_P, L_S, C_P, C_S, M\}$ are searched within the empirically selected lower and upper bounds.

2) Dynamic Frequency Approaching: Based on the aforementioned analysis, it is essential to measure i_P and i_S at multiple frequency points for parameter recognition. However, according to the analysis in Section III-A, when the parameters of the capacitors and coils deviate from the nominal values, the frequency variations near the nominal resonance point may lead to severe system detuning, resulting in enormous coil currents. To constrain the coil currents in a safe range, a dynamic frequency approaching strategy is proposed, as shown in Fig. 12. In Fig. 12, f_L, f_H, and I_M, as well as the update equations (15) and (16), are predesigned based on the system parameters and stored in the microcontrollers in advance. However, the values of I_{P1} and I_{S1} are updated based on the measured results in

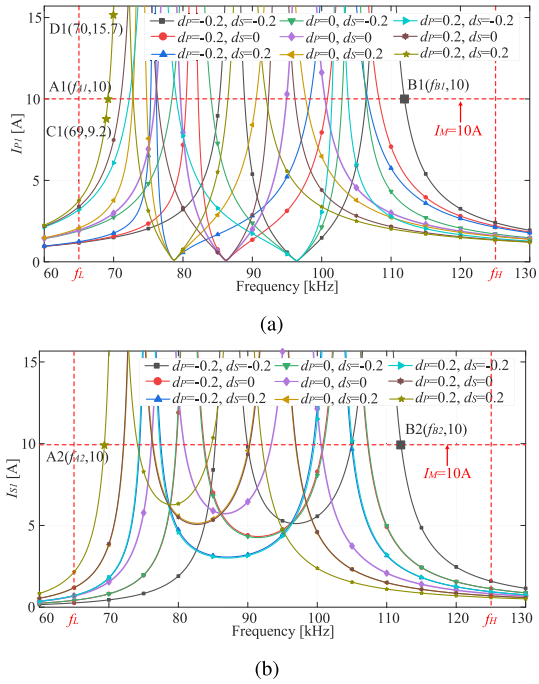

Fig. 13. Values of I_{P1} and I_{S1} when the rectifier output is short-circuited under Case B. (a) I_{P1}. (b) I_{S1}.

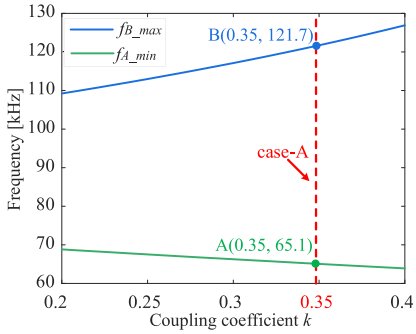

Fig. 14. Values of $f_{A\_\min}$ and $f_{B\_\max}$ under different values of k when the rectifier output is short-circuited.

practical operation. The detailed steps of this strategy are as follows. First, the frequency is swept from the lower bound f_L at various frequency points, while I_{P1} and I_{S1} are measured. The frequency-sweeping process is stopped when I_{P1} or I_{S1} exceeds the threshold value I_M. Then, the frequency is swept from the upper bound f_H and is terminated when I_{P1} or I_{S1} is larger than I_M again.

In this article, the current threshold I_M is set as 10 A based on the current capability of the system, while f_L and f_H are set to 65 and 125 kHz. The basic principle of selecting f_L and f_H is to ensure that I_{P1} and I_{S1} at both f_L and f_H are lower than 10 A under any case. Take Case B as an example, the values of I_{P1} and I_{S1} when the rectifier output is short-circuited is shown in Fig. 13. As illustrated in Fig. 13(a), f_L is required to be lower than f_{A1} to ensure that the value of I_{P1} is smaller than 10 A at the frequency point f_L under any case, while f_H should be higher than f_{B1} to guarantee I_{P1} is always smaller than 10 A at f_H. Similarly, as shown in Fig. 13(b), f_L is also required to be less than f_{A2}, and f_H is needed to be greater than f_{B2} to ensure that the value of I_{S1} does not exceed the threshold. Furthermore, define $f_{A\_\min}$ as the minimum value of f_{A1} and f_{A2}, $f_{B\_\max}$ as the maximum value of f_{B1} and f_{B2}, the values of $f_{A\_\min}$ and $f_{B\_\max}$ under different values of k when the rectifier output is short-circuited is illustrated in Fig. 14. To guarantee the coil currents at f_L and f_H are lower than 10 A under any case, as shown in Fig. 14, f_L is required to be lower than 65.1 kHz, and f_H should be larger than 121.7 kHz. Therefore, f_L and f_H are set to 65 and 125 kHz, respectively.

Moreover, the interval of the frequency points is not fixed but dynamically adjusted according to the measured current values. The motivations of the dynamic frequency interval are as follows. On one hand, when the frequency approaches to the peak current point, the coil currents rise dramatically. Take $d_P = d_S = 0.2$ under Case B as an example, as shown in Fig. 13(a), I_{P1} is 9.2 A when the frequency is 69 kHz, whereas it rapidly increases to 15.7 A at 70 kHz. As a result, if the frequency interval is large under the high-current frequency points, the coil currents may greatly exceed the threshold, endangering the safe operation of the system. On the other hand, when the frequency is close to f_L and f_H, as illustrated in Fig. 13(a), the coil currents might be quite small under some cases, and the measurement errors should be considered in these cases. Therefore, if the frequency interval is small under the low-current frequency points, the measurement errors might be significant in some cases. Besides, a small frequency interval will also make the frequency-sweep process time consuming. Considering the aforementioned reasons, a dynamic frequency interval is adopted in this article. When the frequency is increased from f_L, the update equation is

$$f(i+1) = f(i) + \tau \times \text{ceil}[I_M - \max(I_{P1}(i), I_{S1}(i))] \quad (15)$$

where ceil is the round-up function; τ is a fixed factor, which is set to 0.2 to ensure that the coil current does not increase dramatically as it approaches to the threshold I_M. Similarly, when the frequency is decreased from f_H, the updated equation is

$$f(i+1) = f(i) - \tau \times \text{ceil}[I_M - \max(I_{P1}(i), I_{S1}(i))]. \quad (16)$$

As shown in (15) and (16), the frequency interval is dynamically adjusted between 0.2 and 2 kHz according to the rms values of the coil currents. Based on the aforementioned analysis, by using the proposed dynamic frequency approaching strategy, the coil currents are constrained safely, and the required data for parameter recognition is acquired efficiently.

3) JAYA Algorithm: After the required data are obtained, the optimization problem described in (14) is needed to be solved to recognize the unknown parameters. In this article, a heuristic algorithm called JAYA is introduced to derive the unknown parameters. Generally, there are two mainstream approaches for solving unknown parameters in the WPT systems: the least square approximation (LSA) and the heuristic algorithms. The LSA was implemented in [32] to recognize the mutual inductance and load resistance, while it was used for identifying multiple loads in [27] and the secondary-side reactance in [22]. The heuristic

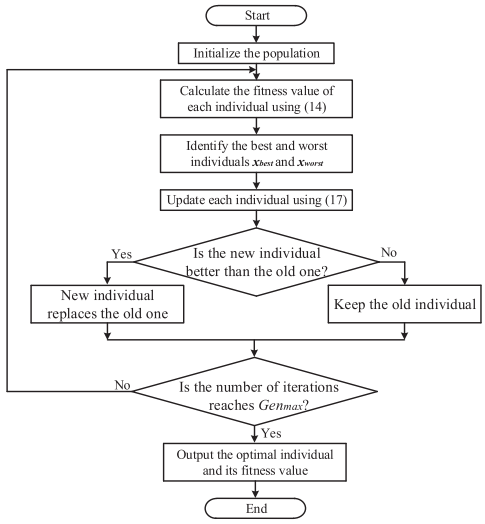

Fig. 15. Flowchart of the JAYA algorithm.

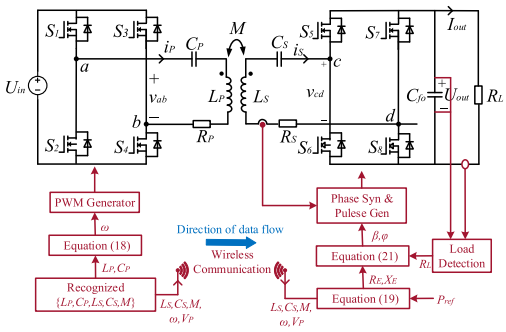

Fig. 16. Block diagram of the impedance tuning method. Herein, the parameters $\{L_S, C_S, M, \omega, V_P\}$ are transmitted from the primary controller to the secondary controller for calculating the required phase shift angles of the active rectifier.

algorithms, which can find optimal solutions more efficiently than the traditional LSA for the multivariable systems [26], are also usually used, such as the GA in [33], and the adaptive differential evolution (ADE) algorithm in [26]. However, for the conventional GA algorithm and differential evolution (DE) algorithm, various algorithm-specific parameters, including the crossover and mutation rates, need to be tuned. Although the ADE algorithm avoids the difficulty of tuning parameters, the adaptive cross-over and mutation rates need to be calculated in each iteration, which increases the complexity of the algorithm. Compared with the GA and ADE algorithms, the JAYA algorithm is free from algorithm-specific parameters (except for two common parameters, i.e., the population size P_{size} and the maximum number of generations $\text{Gen}_{\max}$), and only one update equation is required in each generation [28]. The flowchart of the JAYA algorithm is depicted in Fig. 15, and the process is detailed as follows: *[Initialization]* First, a random population $\boldsymbol{x}$ with P_{size} individuals is generated in the search space (within the lower and upper bounds), where $\boldsymbol{x_{p,q}}$ represents the qth parameter of the pth individual ($p = 1, 2, \ldots, P_{\text{size}}$; $q = 1, 2, \ldots, N$), and N is the number of the unknown parameters. Specifically, in this article, $\boldsymbol{x}$ represents the population with P_{size} (P_{size}=50) individuals, and each individual consists of N (N=7) unknown parameters. The unknown parameters are R_P, R_S, L_P, L_S, C_P, C_S, and M, respectively. *[Fitness]* Then, the fitness value of each individual is calculated based on the cost function described in (14). *[Update]* According to the fitness value of each individual, the best individual $\boldsymbol{x}_{\text{best}} = [x_{\text{best},1}, x_{\text{best},2}, \ldots, x_{\text{best},N}]$ with minimum fitness value and the worst individual $\boldsymbol{x}_{\text{worst}} = [x_{\text{worst},1}, x_{\text{worst},2}, \ldots, x_{\text{worst},N}]$ with maximum fitness value are selected, and the population is then updated by

$$x'_{p,q} = x_{p,q} + r_1(x_{\text{best},q} - |x_{p,q}|) - r_2(x_{\text{worst},q} - |x_{p,q}|) \quad (17)$$

where $x_{\text{best},q}$ and $x_{\text{worst},q}$ are the qth parameter of the best and worst individuals, respectively; r_1 and r_2 are two random numbers within [0,1]. In (17), the term $r_1(x_{\text{best},q} - |x_{p,q}|)$ reveals the tendency of approaching the best individual, whereas the term $-r_2(x_{\text{worst},q} - |x_{p,q}|)$ indicates the tendency of escaping from the worst individual. *[Selection]* The updated individual $x'_{p,q}$ is accepted if it gives a better fitness value. All the accepted individuals at the end of iteration are retained and become the input of the next generation. *[Termination]* The optimization process is stopped when the termination criteria is satisfied. Here, the termination criteria is the number of iterations reaches $\text{Gen}_{\max}$.

C. Impedance Tuning

Based on the recognized parameters, an impedance tuning method is adopted, as shown in Fig. 16. To minimize the primary reactance X_P, the switching frequency ω of the inverter is adjusted to

$$\omega = \frac{1}{\sqrt{L_P C_P}}. \quad (18)$$

Additionally, the duty cycle of the inverter ac voltage v_{ab} is maintained at the full duty cycle. Then, the equivalent load impedance Z_E is regulated by the active rectifier to minimize the secondary reactance X_S and to obtain the required output power P_{ref}, i.e.,

$$\begin{cases} R_E = \dfrac{\omega^2 M^2 P_{\text{ref}}}{V_P^2} \\ X_E = -X_S = -\left(\omega L_S - \dfrac{1}{\omega C_S}\right). \end{cases} \quad (19)$$

Herein, it should be noted that the secondary reactance can be slightly overcompensated to realize zero-voltage-switching (ZVS) for the inverter [22]. According to [18], the equivalent load impedance provided by the active rectifier is

$$\begin{cases} R_E = \dfrac{4}{\pi^2} R_L \cos^2(\varphi)(1 - \cos(\beta)) \\ X_E = \dfrac{4}{\pi^2} R_L \sin(\varphi)\cos(\varphi)(1 - \cos(\beta)) \end{cases} \quad (20)$$

where β is the duty-cycle angle of the rectifier input voltage v_{cd}, and φ is the phase shift angle between $\dot{V}_S$ and $\dot{I}_S$. Substituting (20) into (21), β and φ are derived by

$$\begin{cases} \varphi = \arctan\left(\dfrac{X_E}{R_E}\right) \\ \beta = \arccos\left(1 - \dfrac{\pi^2 X_E}{2 R_L \sin(2\varphi)}\right). \end{cases} \quad (21)$$

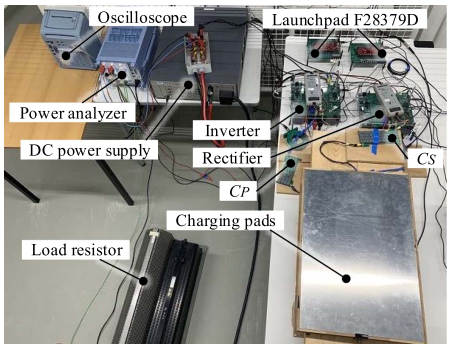

Fig. 17. Experimental setup of the SS-compensated WPT system.

TABLE II
CASE STUDY FOR PARAMETER RECOGNITION

No.	$L_P[\mu\text{H}]$	$L_S[\mu\text{H}]$	$M[\mu\text{H}]$	C_P[nF]	C_S[nF]
A1	335.5	222.7	95	9.9	17.32
A2	335.5	222.7	95	11.53	16.5
A3	335.5	222.7	95	11.53	14.88
A4	335.5	222.7	95	9.9	13.21
A5	335.5	222.7	95	9.07	14.88
B1	327.5	216.5	58	9.9	17.32
B2	327.5	216.5	58	11.53	16.5
B3	327.5	216.5	58	11.53	14.88
B4	327.5	216.5	58	9.9	13.21
B5	327.5	216.5	58	9.07	14.88

Considering the range of β ([0,π]) and φ ([$-\pi/2, \pi/2$]), the maximum R_E and X_E that can be provided by the active rectifier are $8R_L/\pi^2$ and $\pm 4R_L/\pi^2$, respectively.

IV. EXPERIMENTAL VERIFICATION

A. Experimental Setup

To verify the feasibility of the proposed parameter recognition-based impedance tuning method, experiments are carried out on an SS-compensated WPT prototype using the charging pads in Fig. 3, as shown in Fig. 17. A dc power supply is utilized to provide the required power, and two rheostats are connected in series as the load resistor. The impedance tuning algorithm and PWM generation are implemented in the LaunchPad F28379D. Two separate H-bridge converters are adopted as the inverter and the active rectifier, respectively. The experimental data and waveforms are recorded by an oscilloscope (YOKOGAWA DLM2054) and the dc to dc efficiency of the system is measured by a power analyzer (YOKOGAWA WT500). More details of the prototype are listed in Table II.

B. Parameter Recognition

The accuracy of the proposed parameter recognition method is verified in ten cases of the parameter deviations, as listed in Table II. The parameters of the coil inductances and compensation capacitances in Table III are measured by an impedance analyzer (Agilent 4294 A).

To acquire the required data for parameter recognition, the rectifier output is short-circuited and the system frequency f is regulated based on the dynamic frequency approaching strategy

TABLE III
PARAMETERS OF THE JAYA ALGORITHM

Symbol	Value	Symbol	Value
L_{PL}	300 μH	L_{PH}	350 μH
L_{SL}	200 μH	L_{SH}	250 μH
M_L	50 μH	M_H	120 μH
C_{PL}	5 nF	C_{PH}	15 nF
C_{SL}	10 nF	C_{SH}	20 nF
R_{PL}	0.5 Ω	R_{PH}	0.9 Ω
R_{SL}	0.3 Ω	R_{SH}	0.7 Ω
P_{size}	50	$\text{Gen}_{\max}$	5000

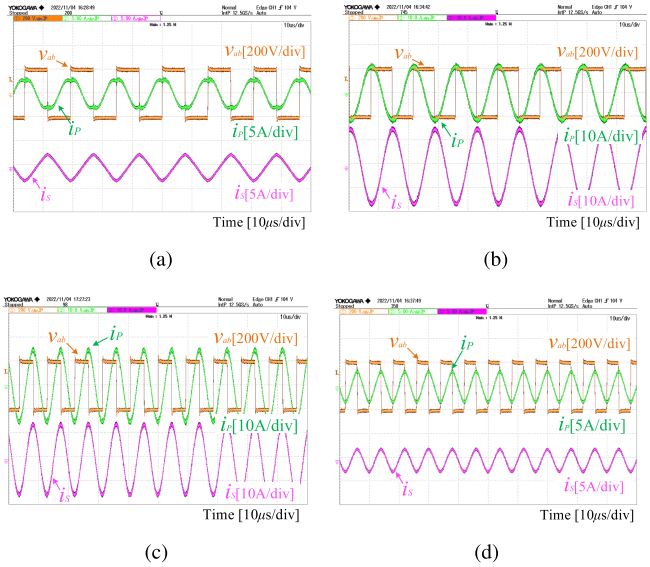

Fig. 18. Measured operating waveforms of Case A1 under different frequency points. (a) 65 kHz. (b) 70.4 kHz. (c) 107.7 kHz. (d) 125 kHz.

shown in Fig. 12. By dynamically adjusting the system frequency f, the primary and secondary coil currents i_P and i_S are measured at multiple frequency points. The measured data are recorded by the oscilloscope, and then, extracted to MATLAB for processing. Fig. 18 shows the recorded waveforms of Case A1 under different frequency points. It should be noted that when the frequency is increased from f_L (65 kHz), hard switching of the inverter power switches is inevitable due to the capacitive input impedance Z_{in}. However, since the data acquisition stage only lasts for hundreds of milliseconds (see Section IV-D), the extra switching loss caused by hard switching during this process can be ignored, and the voltage spikes at the switching transient can also be suppressed by optimizing the *resistor–capacitor* (*RC*) snubber circuits in practice [34], [35]. Another noteworthy point is that the extracted coil currents, as shown in Fig. 18(a), contain a small amount of third harmonics when the frequency is increased from f_L (65 kHz). Therefore, a digital second-order LPF is implemented to filter out the harmonic components of the coil currents when the frequency is increased from f_L, and the magnitude–frequency response of the designed LPF is illustrated in Fig. 19. It should be noted that when the frequency is decreased from f_H (125 kHz), the digital LPF is not required due to the third harmonics are well-attenuated by the high-impedance characteristics of the resonant circuits in the

TABLE IV
COMPARISONS WITH OTHER WORKS ON IMPEDANCE TUNING

Reference	Compensation	Considered parameters	Parameter recognition	Impedance tuning	Wireless communication	Rated Power
[9]	LCC-S	L_P	Phase detection	SCC	No	66.8 W
[20]	LCC-S	M, L_P, L_S	Phase detection	Frequency tuning & semi-active rectifier	No	3.3 kW
[24]	LCC-LCC	M, L_P, L_S	Phase detection & the gradient descent algorithm	Two SCCs	No	3 kW
[21]	SS	C_P, C_S	Phase detection & auxiliary coils	Frequency tuning & semi-active rectifier	Yes	50 W
[22]	SS	L_S, C_S	Pulse density modulation & the LSA algorithm	Frequency tuning & active rectifier	No	145 W
This article	SS	M, L_P, L_S, C_P, C_S	Dynamic frequency approaching & the JAYA algorithm	Frequency tuning & active rectifier	Yes	800 W

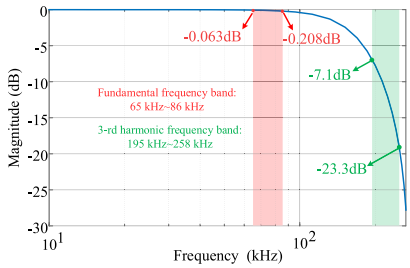

Fig. 19. Magnitude–frequency response of the designed digital LPF. Herein, the maximum frequency point that can be reached when the frequency is increased from f_L is calculated as 86 kHz based on the parameter deviation range listed in Table II.

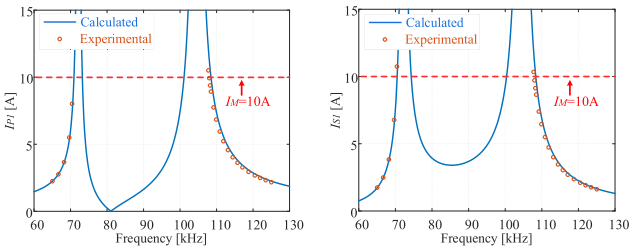

Fig. 20. Extracted rms values of I_{P1} and I_{S1} in Case A1. (a) I_{P1}. (b)I_{S1}.

high-frequency band, as it can be observed in Fig. 18(c) and (d). After the harmonics are filtered by the LPF, the rms values of the fundamental components of the coil currents, i.e., I_{P1} and I_{S1}, are then extracted by the rms function of MATLAB. The extracted rms values of I_{P1} and I_{S1} under Case A1 are illustrated in Fig. 20. As it can be observed, by implementing the proposed dynamic frequency approaching method, I_{P1} and I_{S1} are accurately obtained under sufficient frequency points.

Furthermore, based on the values of I_{P1} and I_{S1}, the JAYA algorithm is implemented to recognize the unknown parameters of the resonant circuits. The searching constraints of the unknown parameters $\{L_P, L_S, M, C_P, C_S\}$ for the JAYA algorithm are listed in Table IV. Since the loss resistances R_P and R_S may vary with the system operating conditions, R_P and R_S are considered as the unknown parameters as well. Additionally, the population size P_{size} and the maximum generation numbers

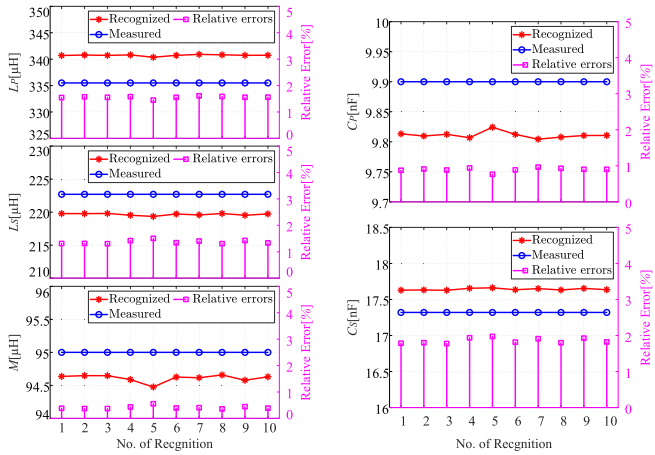

Fig. 21. Recognized results for Case A1. (a) Coil inductances L_P, L_S, and M. (b) Compensation capacitances C_P and C_S.

$\text{Gen}_{\max}$ of the JAYA algorithm are also shown in Table IV. The parameters are independently recognized by the JAYA algorithm for ten times. The JAYA algorithm is implemented in MATLAB on a computer with a Intel(R) Core(TM) i7-1185G7 CPU, and the average computation time for each recognition is 1–3 s. Fig. 21 presents the recognized parameters for Case A1 in each recognition. As shown in Fig. 21, the unknown parameters of Case A1 are recognized accurately, with the relative errors in each recognition all less than 2%. Besides, as it can be observed, the recognized results of each independent recognition are basically consistent, which validates the stability of the JAYA algorithm. Fig. 22 shows the average relative errors (AREs) of Case A1 under different numbers of frequency points. As shown in Fig. 22, the AREs are significant when the number of extracted frequency points is small. This is because when the amount of extracted data is insufficient, it becomes difficult to converge to the optimal solution in the iterative process due to inevitable measurement noise, and the results of each recognition is not stable. This phenomenon can also be observed in other similar works [22], [27]. However, the AREs converge to a stable level as the number of extracted frequency points increases. It should be noted that the number of frequency points can be tuned by

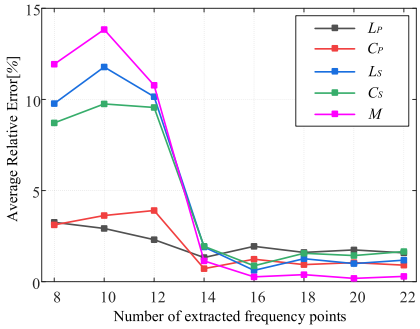

Fig. 22. AREs of Case A1 under different numbers of frequency points.

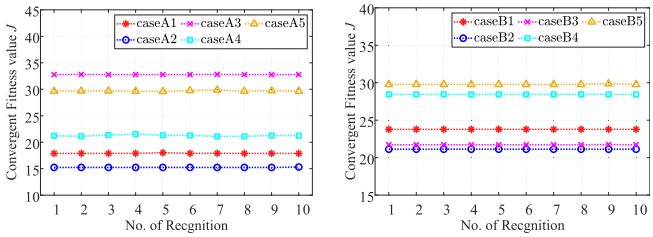

Fig. 23. Convergent fitness values for the studied ten cases. (a) Case A. (b) Case B.

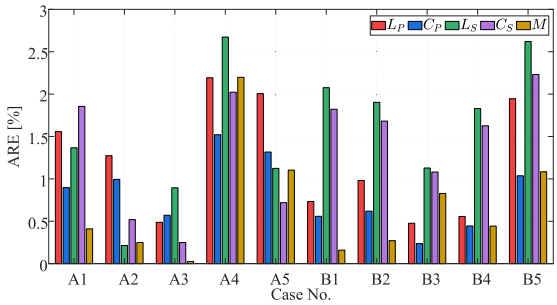

Fig. 24. AREs for the studied ten cases.

tuning the factor τ in (15) and (16) to ensure sufficient frequency points can be obtained for accurate parameter recognition.

Moreover, all of the ten cases listed in Table III are studied. To verify the stability of the JAYA algorithm, the convergent fitness values for all of the studied ten cases are demonstrated in Fig. 23. The convergent fitness values are steady for all cases in each recognition, which validates that the JAYA algorithm can always find the global optimal solution. The AREs for the studied ten cases are then presented in Fig. 24. As shown in Fig. 24, the unknown parameters of the resonant circuits are recognized accurately, with the AREs of all cases less than 3%. Moreover, the standard deviations of the recognized results under each case are shown in Fig. 25. The standard deviations of the unknown parameters L_P and L_S. C_P, C_S, and M are less than 0.5 μH, 0.6 μH, 0.012 nF, 0.035 nF, and 0.2 μH, respectively, with the relative standard deviations all less than 0.3%.

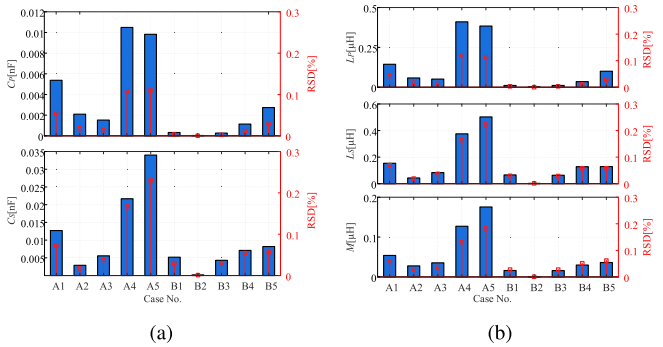

Fig. 25. Standard deviations for the studied ten cases. (a) Coil inductances L_P, L_S, and M. (b) Compensation capacitances C_P and C_S.

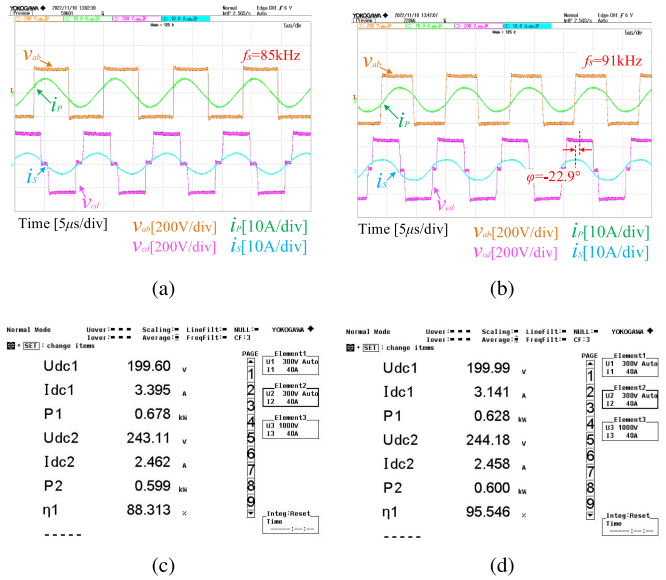

Fig. 26. Measured operating waveforms and dc-to-dc efficiency of Case A5 when delivering 600-W power. (a) Operating waveforms before tuning. (b) Operating waveforms after tuning. (c) Measured dc-to-dc efficiency before tuning. (d) Measured dc-to-dc efficiency after tuning.

C. Impedance Tuning

After the unknown parameters are accurately recognized, the impedance tuning method is implemented to allow the system operate close to the resonance state. To demonstrate the effectiveness of the impedance tuning method, experiments are carried out in two cases of parameter deviations, i.e., Cases A5 and B5. For Cases A5 and B5, the primary and secondary compensation capacitances are 9.07 and 14.88 nF, with the degree of capacitance drift at -13.21% and -5.46%, respectively. Besides, compared with Case A5, the air gap of Case B5 is increased from 10 to 15 cm, and thus, the coil coupling coefficient k is decreased from 0.35 to 0.22. Due to the aforementioned parameter deviations caused by coil misalignment and capacitance drift, both the primary and secondary resonant circuits are detuned.

Fig. 26 presents the measured operating waveforms of Case A5 when delivering 600-W power. Before the impedance tuning, as shown in Fig. 26(a), the system frequency is 85 kHz, and the secondary ac voltage v_{cd} and current i_S are in phase. Moreover,

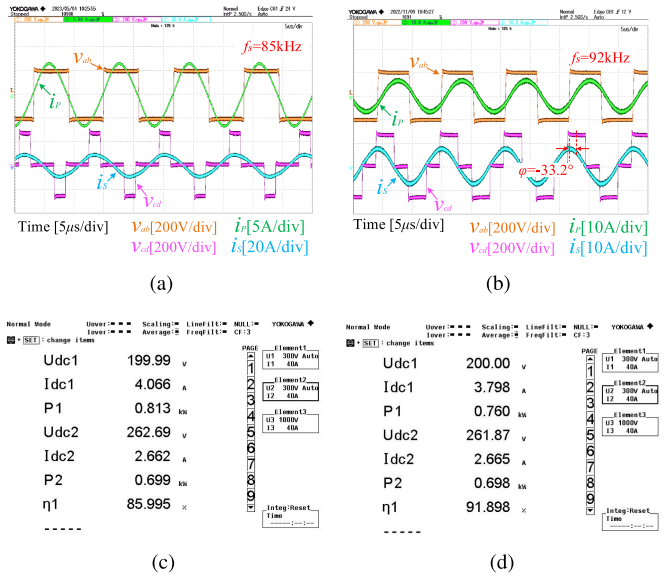

Fig. 27. Measured operating waveforms and DC-to-DC efficiency of Case B5 when delivering 700-W power. (a) Operating waveforms before tuning. (b) Operating waveforms after tuning. (c) Measured DC-to-DC efficiency before tuning. (d) Measured DC-to-DC efficiency after tuning.

due to the system detuning, the primary current i_P leads the primary ac voltage v_{ab}. By implementing the impedance tuning method based on the recognized parameters, the operating frequency is increased to 91 kHz to minimize the primary-side reactance X_P, while the phase shift angle between v_{cd} and i_S, i.e., φ, is regulated to $-22.9°$ to minimize the secondary-side reactance X_S. After the impedance tuning, as illustrated in Fig. 26(b), the primary voltage v_{ab} and current i_P are almost in phase (i_P slightly lags behind v_{ab} to realize ZVS for the inverter). To illustrate the effectiveness of the impedance tuning, the measured dc-to-dc efficiency of Case A5 before and after tuning is further presented in Fig. 26(c) and (d). As it can be observed, when delivering 600 W in Case A5, the dc-to-dc efficiency of the WPT system is increased from 88.3% to 95.5%. The measured operating waveforms and efficiency of Case B5 when delivering 700-W power are then demonstrated in Fig. 27. Based on the identified parameters and carrying out the impedance tuning, as shown in Fig. 27(a) and (b), the system frequency is increased from 85 to 92 kHz, and the phase shift angle φ is adjusted to $-33.2°$. The reactance on both sides are minimized simultaneously, and therefore, the dc-to-dc efficiency of the system is improved from 86% to 91.9%.

Furthermore, the measured dc-to-dc efficiency of Cases A5 and B5 under different output power points is shown in Fig. 28. By implementing the impedance tuning method, the dc-to-dc efficiency is significantly improved. As shown in Fig. 28(a), the efficiency is improved by 4.3%–7.7% after achieving impedance tuning in Case A5. More significant efficiency optimization can be observed under Case B5, as illustrated in Fig. 28(b), the efficiency improvement after tuning ranges from 5.9% to 15%.

It should be noted that due to the parameter deviations in Cases A5 and B5, the output power of the system is limited, as illustrated in Fig. 29. Therefore, Fig. 28 only presents the

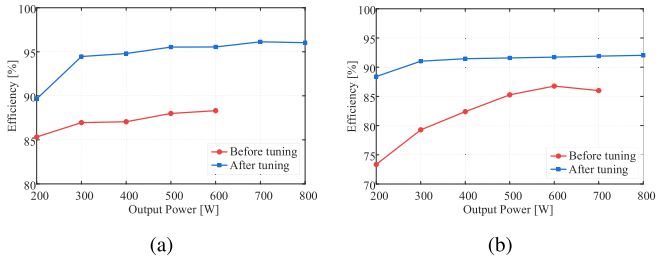

Fig. 28. Measured dc-to-dc efficiency of Cases A5 and B5 under different power points. (a) Case A5. (b) Case B5.

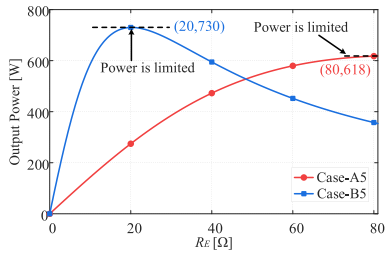

Fig. 29. Illustration of the limited output power due to the parameter deviations under Cases A5 and B5.

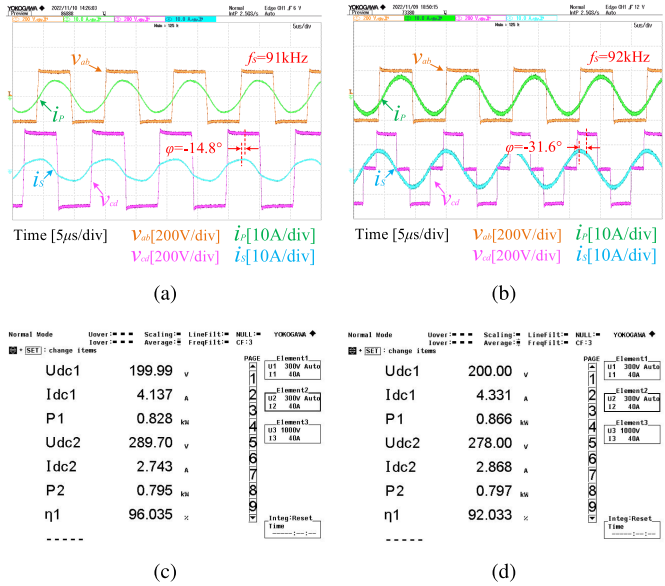

Fig. 30. Measured operating waveforms and DC-to-DC efficiency of Cases A5 and B5 when delivering 800-W power. (a) Operating waveforms after tuning in Case A5. (b) Operating waveforms after tuning in Case B5. (c) Measured DC-to-DC efficiency after tuning in Case A5. (d) Measured DC-to-DC efficiency after tuning in Case B5.

measured efficiency in the power range of 200–600 W before tuning in Case A5, and the measured efficiency in the power range of 200–700 W before tuning in Case B5. Nevertheless, by implementing the impedance tuning method, the system can reach the rated power (800 W) under both Cases A5 and B5, as shown in Fig. 30. As it can be observed, by regulating the system frequency and the phase shift angles of the active rectifier according to the recognized parameters, the system is able to

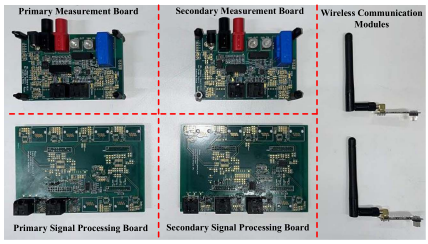

Fig. 31. Hardware modules for the close-loop experiments.

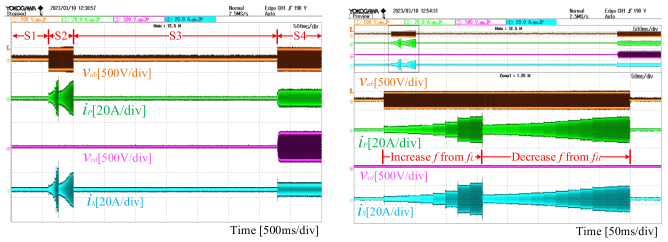

(a) (b)

Fig. 32. Experimental results of the close-loop experiments under Case A5. (a) Complete implementation of the proposed method. (b) Enlarged view of the data acquisition stage.

reach 800-W output power, with the dc-to-dc efficiency at 96% under Case A5 and 92% under Case B5, respectively.

D. Close-Loop Verification

To further verify the feasibility of the proposed method in practice, the close-loop recognition and tuning process is implemented in the TMS320F28379D microcontrollers. Two measurement boards and two signal processing boards, as shown in Fig. 31, are utilized to measure the primary and secondary coil currents, respectively, where the measurement boards are connected to the resonant circuits and the signal processing boards are installed on top of the LaunchPads. Additionally, the NRF24L01+ modules shown in Fig. 31 are employed for the dual-side wireless communication. According to [36], the adopted module takes 339 μs for a single-byte payload to complete a transmission and acknowledgment between the transmitter and the receiver. It is worth noting that the proposed method only requires the measurement of steady-state rms values of the coil currents, and the communication latency does not affect the accurate measurement of these values. Based on the aforementioned hardware modules, the close-loop experiments are carried out under Case A5, where the experimental results are demonstrated in Fig. 32.

As shown in Fig. 32(a), the complete implementation of the proposed method includes four different stages, where S1, S2, S3, and S4 represent the pre start-up stage, the data acquisition stage, the JAYA algorithm execution stage, and the normal charging stage, respectively. After the system starts, it first enters the data acquisition stage, where the rectifier output is short-circuited and the inverter frequency is adjusted based on the proposed dynamic frequency approaching strategy. During this stage, as shown in Fig. 32(b), the inverter frequency f is first increased from f_L, and then, it is decreased from f_H after the coil currents exceed the threshold I_M. The data acquisition stage stops when the coil currents exceed the threshold again. In the experiments, 20 different frequency points are extracted with the time for each frequency point configured at 20 ms, and therefore, the total time for the whole data acquisition stage is 400 ms. After the data acquisition, the JAYA algorithm is implemented to solve the unknown parameters, which takes around 3.2 s in the experiments. In the close-loop tests, the maximum ARE of the recognized results for Case A5 is 2.6%, which is slightly larger than that of using the oscilloscope. The recognition results in the closed-loop experiments are compared with those using the oscilloscope in Fig. 33. The discrepancy in estimated results is attributed to the difference in measurement errors. In the close-loop experiments, the current transducer (LAH 50-P) is adopted to measure the coil currents, with the frequency bandwidth at 200 kHz, and the sampling rate of the DSP is configured at 1 MHz. Compared with the 50-MHz bandwidth of the current probe (KEYSIGHT N2782B) and the 12.5-GHz sampling rate of the oscilloscope, the measurement errors in the close-loop experiments are increased due to the limited bandwidth of the adopted measurement system. Consequently, the recognition errors in the close-loop experiments are slightly larger than that of using the oscilloscope. In practice, the current sensor with high bandwidth and the analog-to-digital converter with high sampling rate can be employed to further minimize the measurement errors, thereby achieving a higher recognition accuracy. Finally, based on the recognized parameters, the system frequency as well as the phase shift angles of the rectifier are regulated to realize the impedance tuning, and the system enters the normal charging stage.

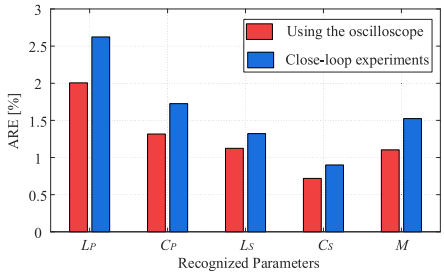

Fig. 33. Comparisons on the recognized results in the close-loop experiments and those using the oscilloscope.

E. Comparison With Other Works

To illustrate the difference between the proposed method and other existing impedance tuning methods, detailed comparisons are summarized in Table IV.

Compared with other reported methods, the main contribution of the proposed method is all parameters of the resonant circuits are recognized simultaneously, without using extra phase detection circuits and auxiliary coils. Based on these identified parameters, the proposed method is able to simultaneously deal with a wide range of parameter deviations caused by capacitance drift and coil misalignment on both sides. In this article, the primary-side reactance is tuned by regulating the inverter frequency, while the secondary-side reactance is tuned by the

TABLE V
COMPARISONS WITH OTHER WORKS ON PARAMETER RECOGNITION

Ref.	Recognized parameters	Data Acquisition & Algorithm	Max. Error	Time
[27]	Multiple loads	Traditional frequency sweeping and LSA	/ [1]	/
[32]	M, R_E	Traditional frequency sweeping and LSA	/	/
[26]	M, R_E, C_S, L_S	Traditional frequency sweeping and ADE	< 3 %	17.95 s
[22]	C_S, L_S	Pulse density modulation and LSA	< 5 %	$2 \sim 5$ s
[37]	M, R_E	Harmonic detection and calculation	6.9 %	7 ms
This article	M, L_P, L_S, C_P, C_S	Dynamic frequency approaching and JAYA	< 3 %	≈ 3.6 s

1 The symbol " / " indicates the relevant details are not provided in the reference.

active rectifier. Compared with those methods using SCCs, the proposed method avoids the extra power losses caused by SCCs. Since all parameters of the resonant circuits are considered, the proposed method requires the secondary-side information to accurately identify L_S, C_S, and M. Therefore, the wireless communication is needed in this article.

Moreover, the proposed method is compared with other existing parameter monitoring methods in Table V. For multi-parameter estimation, it is of great importance to measure the coil currents at various frequency points. The existing methods mainly acquire this information from two distinct perspectives: frequency sweeping [26], [27], [32] and harmonic detection [22], [35]. However, for the harmonic-detection-based methods, the number of parameters that these methods can accurately estimate is restricted by the limited harmonic frequency points. On the other hand, the traditional frequency-sweeping-based methods are susceptible to severe system detuning and load power ripple under wide-range parameter deviations. To this end, a dynamic frequency approaching strategy is proposed in this article, with the rectifier output short-circuited during the parameter recognition process. This approach avoids significant load power ripple, and is able to efficiently and safely measure the coil currents under a sufficient number of frequency points. As shown in Table V, the maximum estimation error of the proposed method is comparable to other existing works. Additionally, the estimation time of the proposed method is around 3.6 s, which is also fast enough for the stationary charging applications.

V. CONCLUSION

In this article, a parameter recognition-based impedance tuning method is proposed for the SS-compensated WPT systems. The proposed parameter recognition method is implemented at pre start-up, with the rectifier output short-circuited during this process. Therefore, the proposed method is more suitable for stationary applications, whereas it is not desirable to be used in the dynamic wireless charging cases. Notably, as the proposed method is load-independent and the total time for the entire process is only several seconds, it can also be repeated during the charging process to deal with some abnormal behaviors, for instance, a sudden movement of the receiver coil or significant variation in operating temperature. Compared with the existing methods, the proposed parameter recognition method avoids severe system detuning and significant load power ripple, and is able to accurately identify all of the unknown parameters of the resonant circuits. The accuracy of the parameter recognition is experimentally validated in ten cases of parameter deviations, with the relative average errors of the recognized results all less than 3%. Thanks to the pre start-up parameter recognition, the parameter deviations caused by coil misalignment and capacitance drift on both the primary and secondary sides can be addressed without adding any extra switches and circuits, which is the main contribution of this proposal. Based on the recognized parameters, an impedance tuning method is carried out to cope with the impedance mismatch caused by parameter deviations. By regulating the system frequency and the phase shift angles of the active rectifier, the reactance on both sides are minimized, and therefore, the dc-to-dc efficiency of the WPT prototype is enhanced by 4.3–15% in the experiments. Close-loop verification is also implemented to further verify the feasibility of the proposed method in practice, with the time consumption for the whole parameter recognition process at around 3.6 s in the experiments.

It is worth mentioning that this article only presents the application in the typical and widely used SS compensation network. However, in recent years, hybrid compensation structures, such as LCC-S, LCC-LCC, etc., are gaining more and more attention. For these hybrid networks, since the number of passive elements is much greater than that of the SS compensation, the implementation of parameter identification is more difficult, and additional information is required to be measured. Considering the increasing popularity of these hybrid structures, the research on how to further extend the proposed method to the hybrid compensation will be regarded as our future work. Another noteworthy point is that, in addition to its application for active impedance tuning, the proposed parameter recognition strategy also shows promise in optimal power flow control and foreign object detection. These potential applications will also be considered as part of our future work.

REFERENCES

[1] S. R. Hui and W. W. Ho, "A new generation of universal contactless battery charging platform for portable consumer electronic equipment," *IEEE Trans. Power Electron.*, vol. 20, no. 3, pp. 620–627, May 2005.
[2] C. R. Teeneti, T. T. Truscott, D. N. Beal, and Z. Pantic, "Review of wireless charging systems for autonomous underwater vehicles," *IEEE J. Ocean. Eng.*, vol. 46, no. 1, pp. 68–87, Jan. 2021.
[3] D. Ahn and S. Hong, "Wireless power transmission with self-regulated output voltage for biomedical implant," *IEEE Trans. Ind. Electron.*, vol. 61, no. 5, pp. 2225–2235, May 2014.
[4] A. Ahmad, M. S. Alam, and R. Chabaan, "A comprehensive review of wireless charging technologies for electric vehicles," *IEEE Trans. Transp. Electrific.*, vol. 4, no. 1, pp. 38–63, Mar. 2018.
[5] P. Machura and Q. Li, "A critical review on wireless charging for electric vehicles," *Renewable Sustain. Energy Rev.*, vol. 104, pp. 209–234, 2019.
[6] G. Zhu, J. Dong, W. Shi, T. B. Soeiro, J. Xu, and P. Bauer, "A mode-switching-based phase shift control for optimized efficiency and wide zvs operations in wireless power transfer systems," *IEEE Trans. Power Electron.*, vol. 38, no. 4, pp. 5561–5575, Apr. 2023.

[7] W. Zhang and C. C. Mi, "Compensation topologies of high-power wireless power transfer systems," *IEEE Trans. Veh. Technol.*, vol. 65, no. 6, pp. 4768–4778, Jun. 2015.
[8] Y. Wang, Z. Yang, and F. Lin, "Design and implementation of wireless power transfer systems with improved capacitor error tolerance," *IEEE Trans. Ind. Electron.*, vol. 69, no. 5, pp. 4707–4717, May 2022.
[9] D.-H. Kim and D. Ahn, "Self-tuning LCC inverter using PWM-controlled switched capacitor for inductive wireless power transfer," *IEEE Trans. Ind. Electron.*, vol. 66, no. 5, pp. 3983–3992, May 2019.
[10] L. Shi, P. Alou, J. Á. Oliver, J. C. Rodriguez, A. Delgado, and J. A. Cobos, "A self-adaptive wireless power transfer system to cancel the reactance," *IEEE Trans. Ind. Electron.*, vol. 68, no. 12, pp. 12141–12151, Dec. 2021.
[11] R. Mai, P. Yue, Y. Liu, Y. Zhang, and Z. He, "A dynamic tuning method utilizing inductor paralleled with load for inductive power transfer," *IEEE Trans. Power Electron.*, vol. 33, no. 12, pp. 10924–10934, Dec. 2018.
[12] Y. Lim, H. Tang, S. Lim, and J. Park, "An adaptive impedance-matching network based on a novel capacitor matrix for wireless power transfer," *IEEE Trans. Power Electron.*, vol. 29, no. 8, pp. 4403–4413, Aug. 2014.
[13] T. C. Beh, M. Kato, T. Imura, S. Oh, and Y. Hori, "Automated impedance matching system for robust wireless power transfer via magnetic resonance coupling," *IEEE Trans. Ind. Electron.*, vol. 60, no. 9, pp. 3689–3698, Sep. 2013.
[14] J. Kim, D.-H. Kim, and Y.-J. Park, "Free-positioning wireless power transfer to multiple devices using a planar transmitting coil and switchable impedance matching networks," *IEEE Trans. Microw. Theory Techn.*, vol. 64, no. 11, pp. 3714–3722, Nov. 2016.
[15] R. W. Porto, V. J. Brusamarello, L. A. Pereira, and F. R. de Sousa, "Fine tuning of an inductive link through a voltage-controlled capacitance," *IEEE Trans. Power Electron.*, vol. 32, no. 5, pp. 4115–4124, May 2017.
[16] M. Moghaddami, A. Sundararajan, and A. I. Sarwat, "A power-frequency controller with resonance frequency tracking capability for inductive power transfer systems," *IEEE Trans. Ind. Appl.*, vol. 54, no. 2, pp. 1773–1783, Mar./Apr. 2017.
[17] A. Namadmalan, "Self-oscillating tuning loops for series resonant inductive power transfer systems," *IEEE Trans. Power Electron.*, vol. 31, no. 10, pp. 7320–7327, Oct. 2016.
[18] R. Mai, Y. Liu, Y. Li, P. Yue, G. Cao, and Z. He, "An active-rectifier-based maximum efficiency tracking method using an additional measurement coil for wireless power transfer," *IEEE Trans. Power Electron.*, vol. 33, no. 1, pp. 716–728, Jan. 2018.
[19] A. Berger, M. Agostinelli, S. Vesti, J. A. Oliver, J. A. Cobos, and M. Huemer, "A wireless charging system applying phase-shift and amplitude control to maximize efficiency and extractable power," *IEEE Trans. Power Electron.*, vol. 30, no. 11, pp. 6338–6348, Nov. 2015.
[20] S. Ann and B. K. Lee, "Analysis of impedance tuning control and synchronous switching technique for a semibridgeless active rectifier in inductive power transfer systems for electric vehicles," *IEEE Trans. Power Electron.*, vol. 36, no. 8, pp. 8786–8798, Aug. 2021.
[21] K. Song et al., "An impedance decoupling-based tuning scheme for wireless power transfer system under dual-side capacitance drift," *IEEE Trans. Power Electron.*, vol. 36, no. 7, pp. 7526–7536, Jul. 2021.
[22] R. Dai, R. Mai, and W. Zhou, "A pulse density modulation based receiver reactance identification method for wireless power transfer system," *IEEE Trans. Power Electron.*, vol. 37, no. 9, pp. 11394–11405, Sep. 2022.
[23] W. Li, G. Wei, C. Cui, X. Zhang, and Q. Zhang, "A double-side self-tuning LCC/S system using a variable switched capacitor based on parameter recognition," *IEEE Trans. Ind. Electron.*, vol. 68, no. 4, pp. 3069–3078, Apr. 2021.
[24] Z. Luo, Y. Zhao, M. Xiong, X. Wei, and H. Dai, "A self-tuning LCC/LCC system based on switch-controlled capacitors for constant-power wireless electric vehicle charging," *IEEE Trans. Ind. Electron.*, vol. 70, no. 1, pp. 709–720, Jan. 2023.
[25] W. Li, Q. Zhang, C. Cui, and G. Wei, "A self-tuning S/S compensation WPT system without parameter recognition," *IEEE Trans. Ind. Electron.*, vol. 69, no. 7, pp. 6741–6750, Jul. 2022.
[26] Y. Yang, S.-C. Tan, and S. Y. R. Hui, "Front-end parameter monitoring method based on two-layer adaptive differential evolution for SS-compensated wireless power transfer systems," *IEEE Trans. Ind. Inform.*, vol. 15, no. 11, pp. 6101–6113, Nov. 2019.
[27] J. Yin, D. Lin, C. K. Lee, T. Parisini, and S. Hui, "Front-end monitoring of multiple loads in wireless power transfer systems without wireless communication systems," *IEEE Trans. Power Electron.*, vol. 31, no. 3, pp. 2510–2517, Mar. 2016.
[28] R. Rao, "Jaya: A simple and new optimization algorithm for solving constrained and unconstrained optimization problems," *Int. J. Ind. Eng. Comput.*, vol. 7, no. 1, pp. 19–34, 2016.
[29] C.-S. Wang, G. A. Covic, and O. H. Stielau, "Power transfer capability and bifurcation phenomena of loosely coupled inductive power transfer systems," *IEEE Trans. Ind. Electron.*, vol. 51, no. 1, pp. 148–157, Feb. 2004.
[30] J. Zeng, S. Chen, Y. Yang, and S. Y. R. Hui, "A primary-side method for ultrafast determination of mutual coupling coefficient in milliseconds for wireless power transfer systems," *IEEE Trans. Power Electron.*, vol. 37, no. 12, pp. 15706–15716, Dec. 2022.
[31] Y. Yang, S. C. Tan, and S. Y. R. Hui, "Fast hardware approach to determining mutual coupling of series–series-compensated wireless power transfer systems with active rectifiers," *IEEE Trans. Power Electron.*, vol. 35, no. 10, pp. 11026–11038, Oct. 2020.
[32] J. Yin, D. Lin, T. Parisini, and S. Hui, "Front-end monitoring of the mutual inductance and load resistance in a series–series compensated wireless power transfer system," *IEEE Trans. Power Electron.*, vol. 31, no. 10, pp. 7339–7352, Oct. 2016.
[33] D. Lin, J. Yin, and S. R. Hui, "Parameter identification of wireless power transfer systems using input voltage and current," in *Proc. IEEE energy Convers. Congr. Expo.*, 2014, pp. 832–836.
[34] Toshiba Electronic Devices and Storage Corporation, "Power MOSFET selecting MOSFETs and consideration for circuit design," 2018. [Online]. Available: https://toshiba.semicon-storage.com/info/application_note_en_20180726_AKX00064.pdf?did=13416
[35] Fairchild Semiconductor, "Resistor-capacitor (RC) snubber design for power switches," 2014. [Online]. Available: https://www.digikey.com/en/articles/resistor-capacitor-rc-snubber-design-for-power-switches
[36] Nordic Semiconductor, "nRF24L01 single chip 2.4 GHz radio transceiver," 2006. [Online]. Available: https://www.sparkfun.com/datasheets/Components/nRF24L01_prelim_prod_spec_1_2.pdf
[37] J. Liu, G. Wang, G. Xu, J. Peng, and H. Jiang, "A parameter identification approach with primary-side measurement for DC–DC wireless-power-transfer converters with different resonant tank topologies," *IEEE Trans. Transport. Electrific.*, vol. 7, no. 3, pp. 1219–1235, Sep. 2021.

Gangwei Zhu (Student Member, IEEE) was born in Hunan, China, in 1997. He received the B.S. degree in electrical engineering from Central South University, Changsha, China, in 2018, and the M.S. degree in electrical engineering from Shanghai Jiao Tong University, Shanghai, China, in 2021. He is currently working toward the Ph.D. degree in electrical engineering with the Delft University of Technology, Delft, The Netherlands.

His research interests include advanced control and modulation for wireless power transfer.

Jianning Dong (Senior Member, IEEE) received the B.S. and Ph.D. degrees in electrical engineering from Southeast University, Nanjing, China, in 2010 and 2015, respectively.

He was a Postdoctoral Researcher with the McMaster Automotive Resource Centre, McMaster University, Hamilton, ON, Canada. Since 2016, he has been an Assistant Professor with the DC System, Energy Conversion and Storage (DCE&S) Group, Delft University of Technology, Delft, The Netherlands. His research interests include electromechanical energy conversion and contactless power transfer.

Francesca Grazian (Student Member, IEEE) received the B.Sc. degree in electrical engineering from the University of Bologna, Bologna, Italy, in 2016, and the M.Sc. and Ph.D. degrees in electrical engineering from the Delft University of Technology, Delft, The Netherlands, in 2018 and 2023, respectively.

Since January 2023, she has been working as an Electrical R&D Engineer with Laser Precision Solutions, Amsterdam, the Netherlands. Her main research interests include Power Electronics and Wireless Power Transfer for battery charging.

Dr. Grazian was the recipient of the Best Poster Award at the ECPE European Ph.D. School in 2022, Gaeta, Italy, and the Best Paper Award at the International Conference on Power Electronics and Motion Control in 2022.

Pavol Bauer (Senior Member, IEEE) received the master's degree from the Technical University of Kosice, Kosice, Slovakia, in 1985, and the Ph.D. degree from the Delft University of Technology, Delft, The Netherlands, in 1995, both in electrical engineering.

From 2002 to 2003, he was with KEMA (DNV GL), Arnhem, The Netherlands, on different projects related to power electronics applications in power systems. He is currently a Full Professor with the Department of Electrical Sustainable Energy, Delft University of Technology, and the Head of DC Systems, Energy Conversion, and Storage Group. He is also a Professor with the Brno University of Technology, Brno, Czech Republic, and an Honorary Professor with the Politehnica University Timisoara, Timisoara, Romania. He has authored and coauthored more than 120 journal articles and 500 conference papers in his field. He is an author or coauthor of eight books, holds seven international patents, and organized several tutorials at international conferences. He has worked on many projects for the industry concerning wind and wave energy, power electronic applications for power systems such as Smarttrafo, HVdc systems, projects for smart cities such as photovoltaic (PV) charging of electric vehicles, PV and storage integration, and contactless charging; and he participated in several Leonardo da Vinci and H2020, and Electric Mobility Europe EU projects as a Project Partner (ELINA, INETELE, E-Pragmatic, Micact, Trolley 2.0, OSCD, P2P, and Progressus) and as a Coordinator (PEMCWebLab.com-Edipe, SustEner, Eranet DCMICRO).

Dr. Bauer is the Former Chairman of Benelux IEEE Joint Industry Applications Society, Power Electronics and Power Engineering Society Chapter, the Chairman of the Power Electronics and Motion Control Council, a Member of the Executive Committee of European Power Electronics Association, and also a Member of the International Steering Committee at numerous conferences.